Northern Arabian Sea variability from TOPEX/Poseidon altimetry data: an extension of the US JGOFS/ONR shipboard ADCP study

Hyun-Sook Kim[a],*, Charles N. Flagg[b], Stephan D. Howden[c]

[a]*Center for Marine Science and Technology, University of Massachusetts, Dartmouth, New Bedford, MA 02744, USA*
[b]*Department of Applied Sciences, Oceanographic Sciences Group, Brookhaven National Laboratory, Upton, NY 11973, USA*
[c]*The Earth System Science Inter-Disciplinary Center, University of Maryland, College Park, MD 20742, USA*

Abstract

Sea-level anomalies (SLA) derived from the TOPEX/Poseidon (T/P) altimetry and inferred geostrophic currents within the northern Arabian Sea were examined for the period from March 1993 through November 1996. The primary objective of this study was to confirm and extend our understanding of the upper-ocean mesoscale variability observed in the shipboard acoustic Doppler current profiler (ADCP) data collected during the US JGOFS/ONR Arabian Sea Expedition (September 1994–January 1996). The accuracy of the T/P altimetry data ($\sim 3\,\mathrm{cm}$ rms) results in an uncertainty in the altimeter-derived velocities comparable to the ADCP measurement error. Thus the T/P data provide a reasonable method for extending studies of the mesoscale dynamics for the region. Comparison of the T/P-derived geostrophic velocities with concurrent ADCP data showed good correlation, with an r^2 between 0.7 and 0.9 and rms differences of $10\,\mathrm{cm\,s^{-1}}$. The T/P data confirm both the overall spatial and seasonal current patterns observed by the ADCP. The monsoonally averaged rms sea-level anomalies indicate a high degree of intraseasonal variation due to the generation of squirts, jets and eddies all along the coast, the variability of which increases in both intensity and areal extent during the Southwest Monsoon. The SLA data indicate a much reduced degree of variability over the shelf. The SLA-derived eddy kinetic energy (EKE) fields are consistent with those derived earlier from the ADCP data in both distribution and magnitude. There is a large increase in EKE to the west and southwest and to a lesser extent to the south and a large area of relatively reduced eddy activity over much of the eastern and northern Arabian Sea. The area of reduced eddy activity coincides with the location of the most intense portions of the oxygen minimum zone found in the northern Arabian Sea. The spatial scales of the eddies responsible for the EKE distribution over the study area range between 200 and 500 km in the nearshore region, decreasing to 100–200 km offshore. While there is significant energy variability in annual and semi-annual time scales, a substantial portion of the energy is found between 50 and 120 days, and the

---

*Corresponding author. Fax: +1-401-789-1932.
E-mail address: hkim@appsci.com (H.-S. Kim).

relative importance of this frequency band increases offshore. Spectra indicate a distinct break in the frequency content of the eddy field at about 15°N, with little energy at less than annual periods south of this latitude. © 2001 Elsevier Science Ltd. All rights reserved.

1. Introduction

The oceanography of the northwestern Indian Ocean is dominated by monsoonal forcing from the low-level, atmospheric Findlater Jet characterized by its seasonally reversing direction and persistent high speeds ($> 10 \, \mathrm{m \, s^{-1}}$) (Krishnamurti, 1981). The influence of this atmospheric forcing on the ocean is conspicuous, such as the reversals of the eastern and western coastal boundary flow (Schott, 1983; Shetye and Shankar, 1991) as well as the seasonal appearance of the North Equatorial Current (Pickard and Emery, 1990). However, the northern Arabian Sea, despite being located squarely in the path of the Findlater Jet, does not appear to show a similar large-scale current response aside from coastal upwelling. This is evident in a recent study based upon shipboard acoustic Doppler current profiler (ADCP) data (Flagg and Kim, 1998). During the US JGOFS/ONR Arabian Sea Expedition (September 1994–January 1996), Flagg and Kim (1998; hereafter FK98) found, counter to expectation and historical analyses from ship-drift data (Cutler and Swallow, 1984; Hastenrath and Greischar, 1991), that the upper-ocean currents of the northern Arabian Sea were dominated by mesoscale eddies with spatial scales of between 300 and 400 km rather than seasonally reversing currents. A compelling result was that within and above the thermocline, the kinetic energy due to the eddy activity exceeded the mean kinetic energy by more than a factor of 8. The highest eddy currents were found close to the Omani coast and were surface intensified with the energy decreasing with offshore distance and depth. Upper-ocean currents tended to be substantially larger than the record means, which ranged from approximately 5 to 20 cm s^{-1}, and showed little evidence of coherence with the wind stress except near the coast. The mesoscale eddy character of the current field was maintained throughout the year.

The purpose of this paper is to confirm the findings of FK98, particularly the lack of clear seasonal current signal in response to the monsoonal forcing over most of the northern Arabian Sea, by analyzing several years of TOPEX/Poseidon (T/P) repeat ground track altimetry data. We extend and expand upon the ADCP current observations from FK98 with an analysis of the T/P sea-level anomaly (SLA) and SLA-derived geostrophic velocity data collected for the period March 1993–November 1996. The ADCP data were collected during a total of 18, approximately month-long, cruises to the northern Arabian Sea. Seven of the cruises generally followed the cruise track shown in Fig. 1, another four concentrated on sampling only along the "southern" transect, while the remainder were mooring deployment/retrieval cruises. The horizontal resolution of the ADCP was as small as 1.5 km, but was inevitably subject to space/time aliasing and limited areal sampling. By contrast, the T/P sampling covered a large area with along-track resolution of ~ 5.7 km, small relative to the eddy scale, and extended over several years with a temporal resolution of 9.92 days, compared to the monthly cruises. Using these capabilities, we hope to resolve the seasonal fluctuations with greater confidence than we were able to do with the ADCP, and also confirm the dominant spatial scales derived from the ADCP data. Furthermore, the
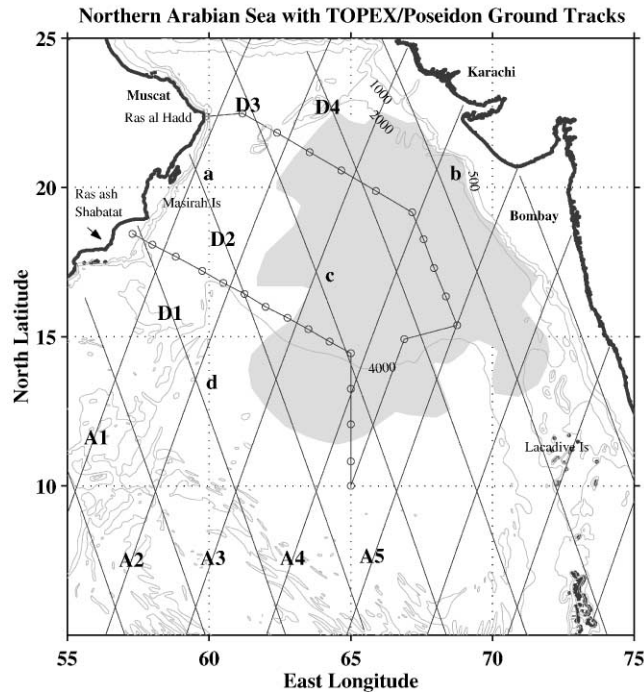
Fig. 1. The Arabian Sea study area: Thin lines are the TOPEX/Poseidon ascending "A" and descending "D" altimeter ground tracks running almost parallel to the Omani coast and Pakistan/Indian coasts, respectively. Also shown is one of the standard cruise tracks of the US Joint Global Ocean Flux Study (JGOFS) that took place from September 1994 to January 1996. The northern and southern transects, referred to in the text, refer to the parallel sections extending offshore from the Omani coast. The lightly shaded region shows the extent of the semi-permanent secondary nitrite maximum from Naqvi (1991) as depicted by Morrison et al. (1998). Points marked with "a"–"d" will be referred to in the text.

long-term and wide areal coverage of the remotely sensed data may bring insight into the annual and interannual variations encompassing the whole of the Arabian Sea.

2. Data and methods

2.1. Altimeter data

For the first few years following the availability of T/P altimeter data, attention was focused on data quality (Nerem et al., 1994) and assimilation into numerical prediction of ocean circulation (Blayo et al., 1994; Smedstad and Fox, 1994). Lately, use of the data has advanced to global- and basin-scale studies (Stammer, 1997a). Recent studies have focused on mesoscale dynamics (Strub et al., 1997), which require greater accuracy because the signal-to-noise ratio tends to degrade as the length scale of interest decreases. The sea-surface elevation data being used for this study are from the repeat-track altimetry collected by the TOPEX and Poseidon (T/P) altimeters obtained from the Goddard Distributed Active Archive Centers of NASA. The altimeter data had been

already adjusted and corrected using processing algorithms developed under a joint effort by NASA and NOAA for the reprocessing of all the existing satellite data, the NASA/GSFC Oceanic Altimeter Pathfinder project. For details of the data processing, refer to Koblinsky et al. (1998). Accuracy of data has drastically improved over the years and currently has an rms error of ~ 3 cm, owing largely to increased precision of the on board instruments and global and regional tidal models (Koblinsky et al., 1998).

Although the ~ 3 cm rms error is generally considered sufficient for purposes of estimating altimeter-derived geostrophic velocities (Strub et al., 1997), minimizing the associated uncertainty is critical. The estimation of the sea-surface slope through finite differencing should be considered carefully, because measurement error and noise propagate and often augment through the derivative operation. The error in the estimate increases by a factor of Δ^2 as the finite-difference spacing Δ decreases. Since the derivative operator acts as a high-pass filter, uncertainty in result amplifies about by a factor of $\kappa/(\sqrt{2}\,2\pi)$ (where $\kappa = 2\pi/\Delta$). By balancing these effects optimally, a minimum total error associated with the derivative estimate can be determined. For the T/P cross-track velocity estimate, total estimated uncertainty is found to have a magnitude of 7 cm s^{-1} at $\Delta = 60$ km (see the appendix for more details), resulting in a comparable velocity uncertainty to that attainable from ADCP measurements (FK98).

The repeat interval for the T/P ground tracks, and hence the temporal resolution of the sea-level data, was 9.9156 days while the along-track resolution was between 5.7 and 5.8 km, depending upon latitude. A total of 14 tracks, seven each ascending and descending (denoted as A's and D's, respectively), cover the northern Arabian Sea from 10 to 25°N latitude and from 55 to 80°E longitude (Fig. 1). The approximate length for the individual tracks ranges from 1000 km for the most southwestern track (D1) to 1780 km for the coastal track (A1).

The altimetry data actually started in September 1992, but there were a number of record gaps in the early portion of the T/P mission (September 1992–February 1993). Thus, cycles 1–16 were excluded from this analysis. The T/P altimetry data spanned a 45-month period from March 1993 to November 1996 (cycles 17–150), which included the time of the US JGOFS/ONR Arabian Sea Expedition (September 1994–January 1996). The occasional gaps in the series were filled with a simple linear space and time interpolation. Since an accurate marine geoid was not available, the data are presented in terms of a sea-level anomaly (SLA) from the 45-month mean elevation at each point along each track.

The spatial distribution of the rms SLA values for the entire period (Fig. 2) indicates that the observed SLA variations are substantially larger than the inherent T/P altimeter noise. However, before we can use these data to make inferences about upper-ocean velocity, we need to understand the SLA variation due to thermal expansion/contraction of the water column.

Results from CTD observations along the two transects during the US JGOFS project showed that the mixed-layer depth ranged from 75 to 100 m during both monsoonal seasons (Gundersen et al., 1998). Using temperature data at ~ 6 m taken from the Arabian Sea project's shipboard ADCP data set together with a thermal expansion coefficient of 1.6×10^{-4}°C^{-1} (Stammer, 1997b), the steric anomaly along the ship tracks can be estimated assuming similar temperature changes over the upper 100 m. Fig. 3 shows the resulting steric estimates, where contours were obtained by linear interpolation in time (y-axis). The steric fluctuations along the northern and southern offshore transects range from -5 to $+4$ cm, which are slightly larger than those found in the Indian Ocean south of 20°N by Stammer (1997b), but are slightly smaller than the values (-7 to
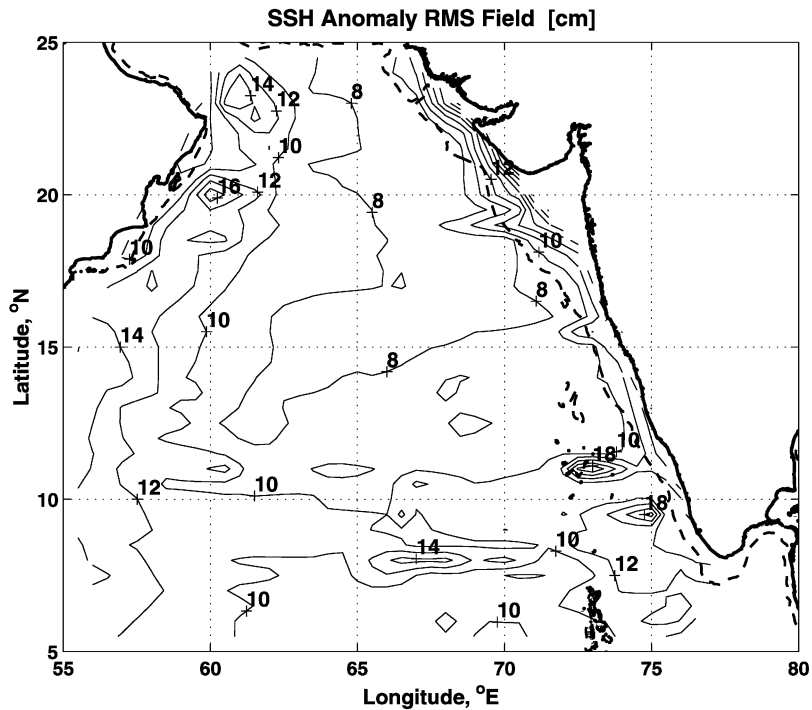
Fig. 2. The distribution of root-mean-square sea-level anomalies for the entire 45-month period of sea-level data. The contours have been linearly interpolated onto $1/2°$ grids from the ascending and descending track lines of Fig. 1. Contour intervals are 2 cm. The heavy dashed contour indicates the 200 m isobath approximately defining the shelf break.

5 cm) found in the upper 500 m using CTD observations from six transits along the two US JGOFS transects. The extreme values were generally found near shore, and appear to be related to coastal upwelling and the effects of nearshore jets and eddies. In the central Arabian Sea, the seasonal steric anomalies were smaller, typically ± 3 cm. Along the nearshore portion of the two transects, the dominant steric variation had an annual period while farther offshore in the central Arabian Sea, a semi-annual fluctuation dominated. This semi-annual steric signal reflects the combined effects of solar insolation, evaporative cooling, and monsoonal wind mixing as evident from the results from the central US JGOFS/ONR mooring located at $15.5°N$, $61.5°E$ (Rudnick et al., 1997; Weller et al., 1998). Over the central and offshore portions of the southern transect, the surface temperature minimum during the Southwest Monsoon (June–September) is an outgrowth of the deepening of the mixed layer, despite the increased heat flux into the ocean. That this second temperature minimum does not show up particularly along the northern US JGOFS transect reflects the limited northeastward extent of the strongest portion of the Southwest Monsoon (Weller et al., 1998).

The relative importance of the steric variations of the seasonal mixed layer on the T/P data also can be assessed from their impact on the observed SLA annual and semi-annual spectral estimates. If we assume that the average annual or semi-annual steric effect is approximately ± 3 cm as suggested by Fig. 3, the variance associated with those fluctuations will be about $4.5 \, cm^2$ and the contribution to the spectral energy density estimates at those periods, with a bandwidth of
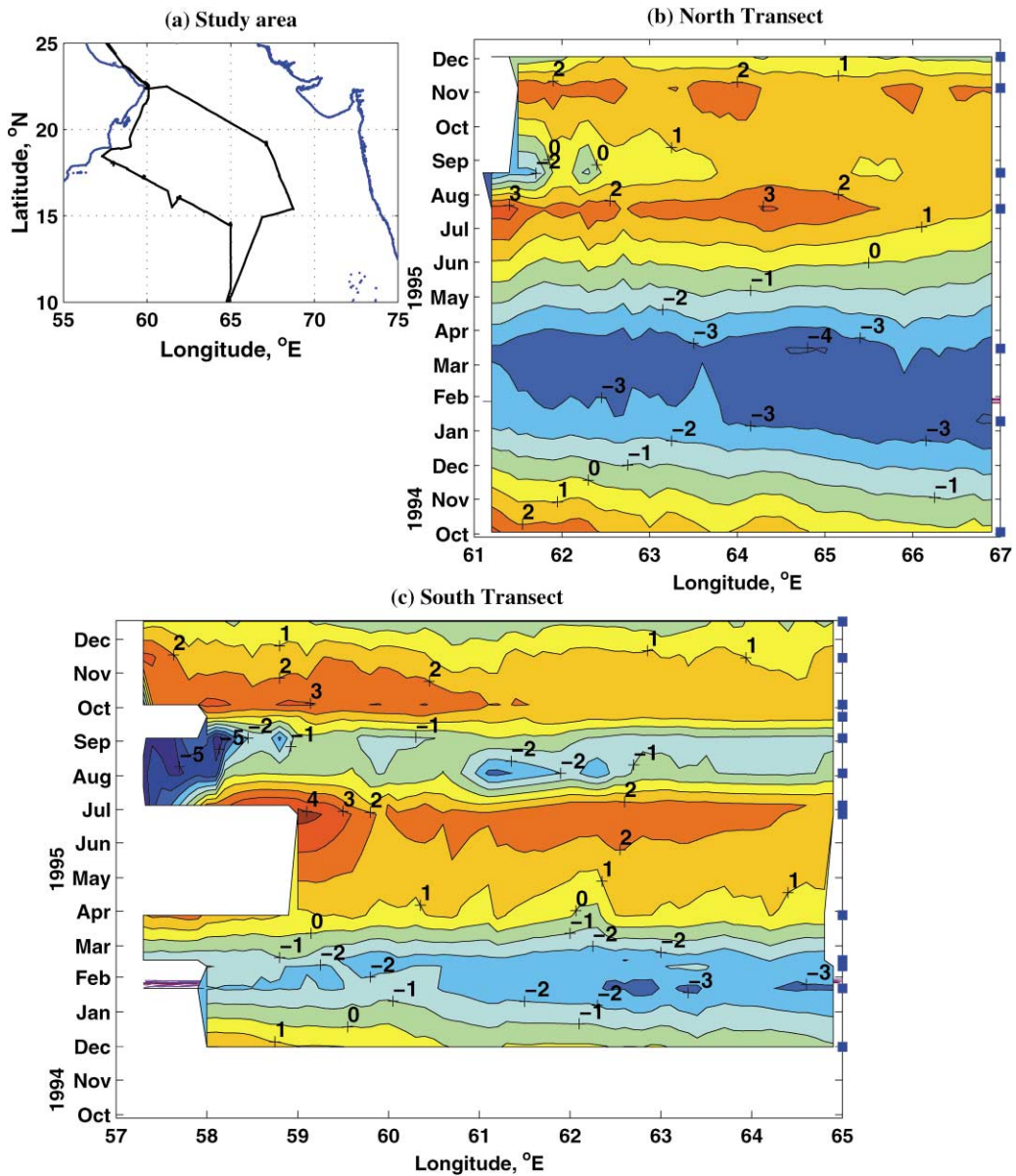
Fig. 3. Estimates of steric height anomalies along the north and south US JGOFS transects shown in the upper-left panel. The contouring is based upon temporal interpolation of 7 and 13 transits (marked by solid squares along the *y*-axis) of the north and south transects, respectively. Contour intervals are 1 cm.

$1/(133 \times 9.9$ days), will be about $5.9 \times 10^3 \, \mathrm{cm}^2 \, \mathrm{cpd}^{-1}$. As shown below, the SLA spectral energy density at these periods is about 18×10^3 and $9 \times 10^3 \, \mathrm{cm}^2 \, \mathrm{cpd}^{-1}$, respectively. Thus, the steric contributions to SLA variability will have little effect at annual periods but may have a more noticeable effect at the semi-annual period. At other periods, the effect should be minor. Because

the spatial scale of the steric effect is nearly equal to the size of the Arabian Sea basin itself, steric contributions should be negligible for the SLA wave number spectra as well as velocity estimates inferred from SLA data.

2.2. Velocity calculations

For the purpose of comparing the altimetry data directly with the ADCP results, upper-ocean velocity anomalies were calculated assuming a geostrophic balance. The cross-track upper-ocean velocity estimates were derived from the along-track SLA profile, η, using

$$V = \frac{g}{f}\frac{d\eta}{dl}, \tag{1}$$

where g is the acceleration of gravity, f is the local Coriolis parameter, and $d\eta/dl$ is the along-track gradient of η. The sign convention adopted for the velocity V is such that V_a is positive to the northwest (292°T) at a right angle to the ascending track, and similarly, V_d is positive toward the northeast (68°T) for the descending track.

At crossover points where ascending and descending tracks intersect, the total surface-geostrophic velocity anomaly, $\vec{V}_g$, can be determined from the non-orthogonal cross-track velocities V_a and V_d. Because the two components are the projections of $\vec{V}_g$ normal to the ground tracks, the orthogonal components of $\vec{V}_g = (u_g\hat{i} + v_g\hat{j})$ may be expressed by the simple geometric transformations

$$u_g = \frac{-V_a + V_d}{2\cos\theta}, \tag{2}$$

$$v_g = \frac{V_a + V_d}{2\sin\theta}, \tag{3}$$

where u_g and v_g are the east and north components, respectively, and θ is the angle the T/P tracks make, relative to north.

Because the differential operator in Eq. (1) behaves like a high-pass filter, the measurement noise in η is amplified during the V computation. To reduce the noise amplification in V, the altimeter data were smoothed prior to the velocity estimation. The choice of the filter parameters was based upon an examination of the wave number velocity spectra that showed a marked increase in noise for wavelengths shorter than about 75 km. Thus, the SLA data were first low-pass filtered with a second-order, forward and backward Butterworth filter with a 75 km cut-off prior to the computation of V.

Uncertainty δV associated with the cross-track velocity estimate V can be determined from the error propagation through the centered difference formulae of Eq. (1) (Eq. (A.1) in the appendix). The total uncertainty δV consists of two components. One is a truncation error associated with the difference approximation equation (A.1), and the other is measurement error, $\delta\eta$, propagated through the derivative operator. With an optimal choice for the interval over which the finite difference is calculated (see the appendix), δV is estimated to have a magnitude of about $7\,\mathrm{cm\,s^{-1}}$.
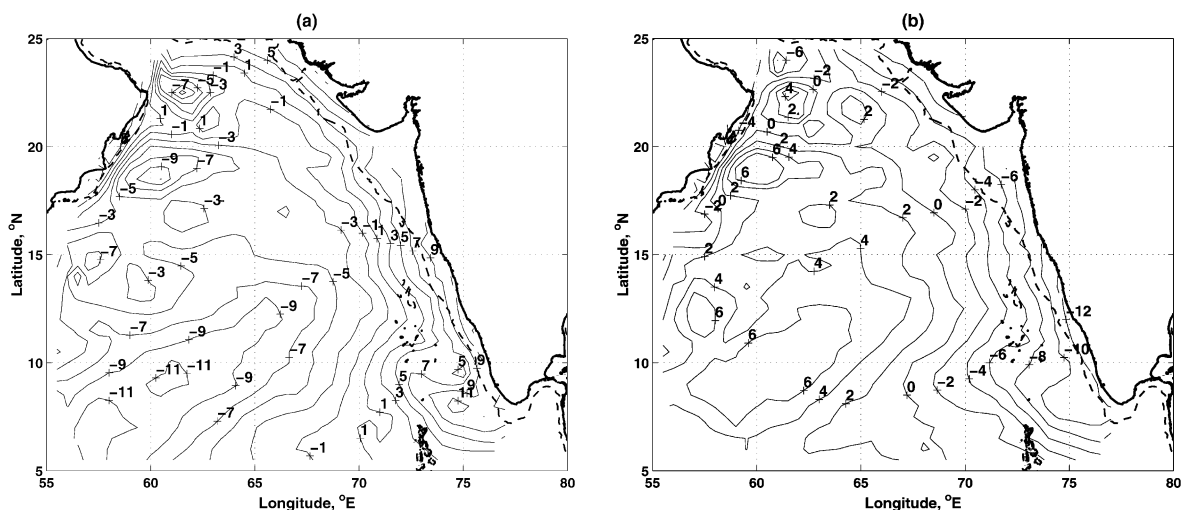
Fig. 4. Seasonally averaged sea-level anomalies during (a) the Northeast Monsoon (November 1–February 15), and (b) the Southwest Monsoon (June 1–September 15). The contours are drawn in the same manner as in Fig. 2. The contour interval is 2 cm.

This value agrees well with the error estimate found with an alternate method in Strub et al. (1997). Assuming that the surface-geostrophic velocity component errors, δu_g and δv_g, are independent, the total uncertainty for the SLA-derived velocity, δV_g, is estimated to be about $14 \, \text{cm s}^{-1}$. The crossover time difference between ascending and descending tracks, which is never more than 5 days, also could introduce errors if the upper-ocean time scale were of a comparable size. However the time-lagged correlation of the T/P-derived velocities from the crossover points indicates a zero crossing of ~ 40 days. This suggests that higher frequency motions should not unduly degrade the velocity estimates from the SLA data.

3. Sea-level variability

One conclusion from the Arabian Sea project's ADCP measurement effort was that there was not a large-scale coherent response of the upper-ocean currents to the monsoonal winds. Contrary to the impression gained from earlier ship-drift data (Cutler and Swallow, 1984; Hastenrath and Greischar, 1991), the ADCP data indicated that the currents in the northern Arabian Sea were dominated by relatively short-term variability and that there was little evidence for downwind near-surface currents, except for the area near and over the continental shelf of the Arabian Peninsula. In the present study, without an accurate geoid, we are unable to look at the long-term mean current field using the sea-level data. However, we can examine the seasonal variations under the strong atmospheric forcing and can see if there are substantial, large-scale changes in currents in response to the strong forcing.

Ship-drift data indicate large-scale, seasonal current fluctuations of $\pm 0.2 \, \text{m s}^{-1}$, implying sea-level slope of $\pm 10^{-6}$ at 20°N, or sea-level changes of $\pm 10 \, \text{cm}$ over 100 km. Fig. 4 shows the
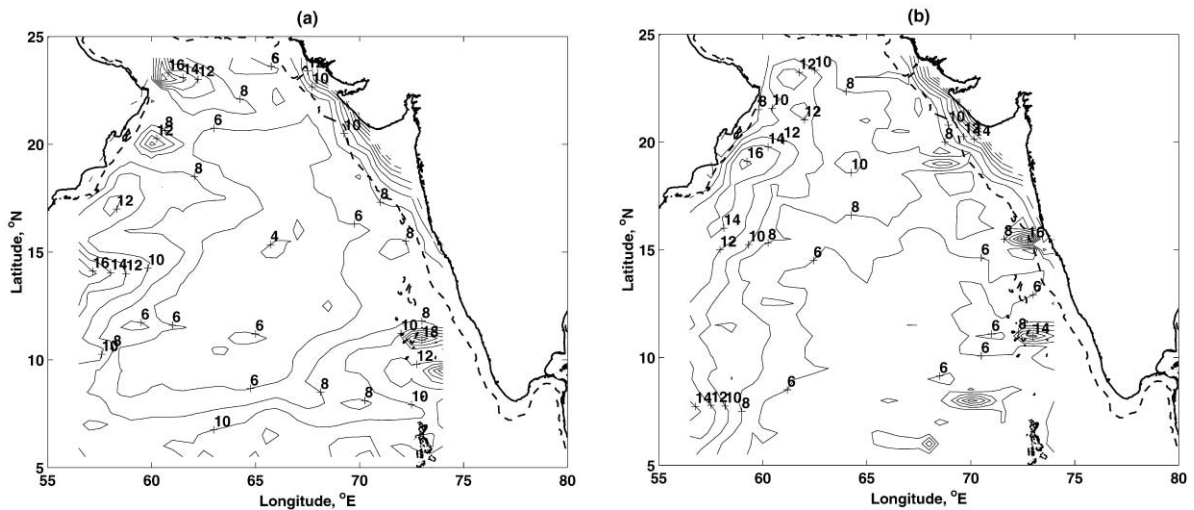
Fig. 5. The distribution of root-mean-square sea-level anomalies for (a) the period of the Northeast Monsoon, and (b) the period of Southwest Monsoon. Contour intervals are 2 cm.

mean SLA in the northern Arabian Sea during the Northeast Monsoon (Fig. 4a), November 1 − February 15, and during the Southwest Monsoon (Fig. 4b), June 1 − September 15. While a substantial fraction of the difference between the mean fields can be ascribed to steric effects as discussed earlier, the apparent responses to the wind forcing stand out above those expected changes. The only areas where sea-level slopes are equivalent to those postulated by the ship-drift estimates are along the Arabian Peninsula during both seasons and along the Indian coast during the Northeast Monsoon (Shetye et al., 1991). Elsewhere, the sea-level slopes are significantly less with typical values on the order of 1 cm over 100 km, equivalent to $2 \, \text{cm} \, \text{s}^{-1}$. In addition to these large-scale characteristics, the seasonal mean anomalies indicate the presence of eddy-like structures along the Arabian Peninsula. During the Northeast Monsoon, there is a relatively intense cyclonic feature off Ras al Hadd indicating southeastward flow along the northeast coast of Oman continuing offshore as the Ras al Hadd Jet. During the Southwest Monsoon, there exists a weak anticyclonic feature in this area suggesting weaker and less organized currents. The oscillation between these two features and their relative magnitudes agrees with the ADCP observations in FK98 and Böhm et al. (1999). Over the rest of the interior of the northern Arabian Sea there are two seasonally reversing gyres, a small one off the Arabian Peninsula and a large gyre in the southwestern portion of the area. The lull between these gyres occurs east of Ras ash Shabatat, the area where the offshore flow of the Shabatat Anticyclone was found (FK98) and close to the origin of some of the filaments detected during extensive SeaSoar surveys (Brink et al., 1998; Lee et al., 1999).

   In order to illustrate further the spatial and seasonal dependence of sea-level variations, rms SLAs were computed for the Northeast and Southwest Monsoons. Fig. 5 shows the resultant seasonal rms fields smoothed with a 75 km low-pass filter and linearly interpolated to a 1/2° grid. The high rms SLA values along the Indo-Pakistani coast are confined to the continental shelf and

appear to represent limitations in the global tidal model used to detide the T/P data. Otherwise, the highest SLA variability is present within 400 km of the Omani coast and off Ras al Hadd during both seasons and south of 8°N during the Northeast Monsoon. Within these areas, the rms SLA are greater than 10 cm, reaching maximum values of 16 cm with a greater overall level of variability during the Southwest Monsoon. The high coastal rms values are located in an area north of the Findlater Jet's axis (Bruce, 1983). This indicates a coupling between strong local wind forcing and the coastal boundary condition, resulting in the generation of coastal squirts, jets and eddies. Minimum rms SLA values are found in the central portion of the northern Arabian Sea with values that range between 4 and 6 cm in both seasons.

Despite the overall similarity of the two seasonal rms SLA distributions, there are some distinct differences, in particular along the southern boundary and in the area of the Laccadive Islands. The high values in the zonal band south of 8°N is a reflection of the seasonal expansion and meanders of the westward flowing North Equatorial Current. In the vicinity of the Laccadives, studies by Shankar and Shetye (1997) and Bruce et al. (1998) indicate that a topographic high forms during the onset of the Northeast Monsoon, which later propagates westward into the Arabian Sea as planetary waves.

Another view of the space/time distribution of SLA variability is afforded by frequency spectra arranged according to latitude for some of the ascending and descending T/P tracks (Fig. 6). Because the tracks cross at an angle of about 44°, the spectra afford a view of two, non-orthogonal traverses of the ocean topography. The path of the nearly shore-parallel A1 track varies between 40 and 200 km offshore, while track A2 is ~ 300 km farther offshore. The descending tracks D2 and D3 originate from the eastern part of the Arabian Peninsula and the Gulf of Oman, respectively. Focusing first on the ascending tracks, the offshore decrease of energy between A1 and A2 (Fig. 2) is quite apparent, and it is also apparent that the offshore energy decrease has little latitudinal dependence. For the inshore track, A1, there are clear annual and semi-annual spectral peaks, as well as a scattering of peaks occurring at two- and four-month periods. There is an interesting energy gap between 20 and 23°N along the nearshore track, which corresponds to the area of the coast between Masirah Island and Ras al Hadd. In this area, the T/P track line runs within 20–30 km of the shelf break, which may restrict the on–offshore velocity to some extent, and hence the along-coast sea-level fluctuations. This is also an area where upwelling during the Southwest Monsoon should be near a maximum, bringing colder water to the surface and reducing seasonal steric effects. According to the underway sea-surface temperature data presented by Morrison et al. (1998a), the annual temperature changes in this area were rather muted. This may explain the lack of annual and semi-annual fluctuations in this area, but it does not address the lack of higher frequency fluctuations. Just to the southwest of this area, in a region where the US JGOFS/ONR ADCP data indicated the presence of strong filaments and eddies (FK98; Lee et al., 1999), semi-annual and shorter period fluctuations were quite energetic. North of the low-energy area, beginning at Ras al Hadd, there is another energetic area that reflects the monsoonal response of the Ras al Hadd Jet and its asymmetric seasonal behavior (FK98; Manghnani et al., 1998; Böhm et al., 1999). Farther offshore along the A2 track, the annual signal is generally present, in particular near 19°N, which corresponds to the strong annual peak along A1. It is noteworthy that there is little energy along A2 at the semi-annual period, but there is considerable energy at periods in the two- to five-month band. For these shorter period oscillations, there is a latitudinal dependence in the dominant period, increasing from about 80
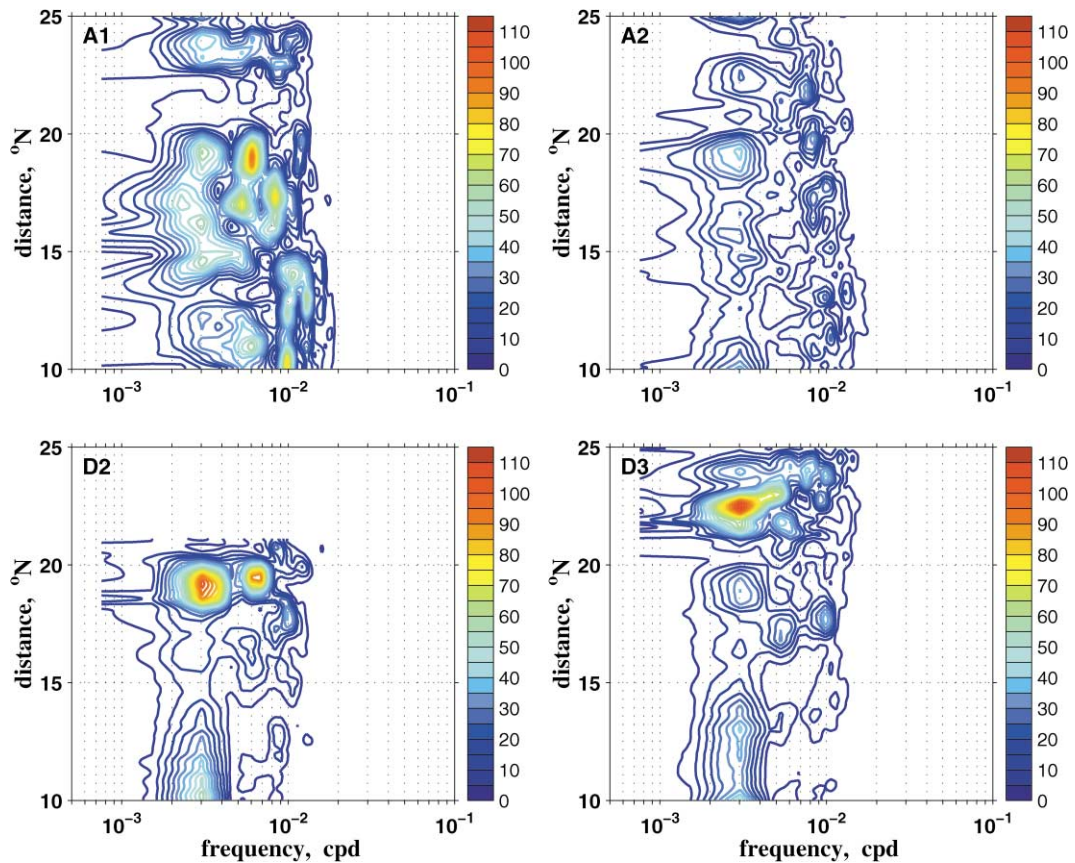
Fig. 6. Latitude-dependent, variance-conserving frequency spectra contours for the ground tracks A1, A2, D2, and D3. The horizontal coordinate is frequency, the vertical coordinate is latitude. The contour interval is $5\,cm^2\,s^{-2}$. The data used for the computation were low-pass filtered with cut-off scales of 75 km and 65 days.

days at $10°N$ to about 120 days at $25°N$. The cause of this latitudinal dependence is unknown at present.

   The temporal spectra from the descending tracks D2 and D3, Fig. 6, show a couple of interesting north–south changes in SLA energy distribution. The descending tracks D1 (not shown) and D2 both show a concentration of energy near the coast at annual and semi-annual periods in keeping with the spectra from the A1 track. Along D2, there is an abrupt drop in energy north of $20°N$, as the track nears the continental shelf; this occurs in the same location as the spectral gap identified along A1. Along D3, which is located further east, the annual signal is especially strong northeast of $20°N$ and Ras al Hadd, peaking in an area that is dominated by the Ras al Hadd Jet as mentioned above. Especially interesting in these descending spectra is the behavior south of about $15°N$. In this area, the annual signal is strong, intensified to the south, and appears to reflect the behavior of the seasonal North Equatorial Current. Note that there is little energy south of $15°N$ at shorter than annual periods, suggesting a distinctive break in the dominant physical processes north and south of this latitude.
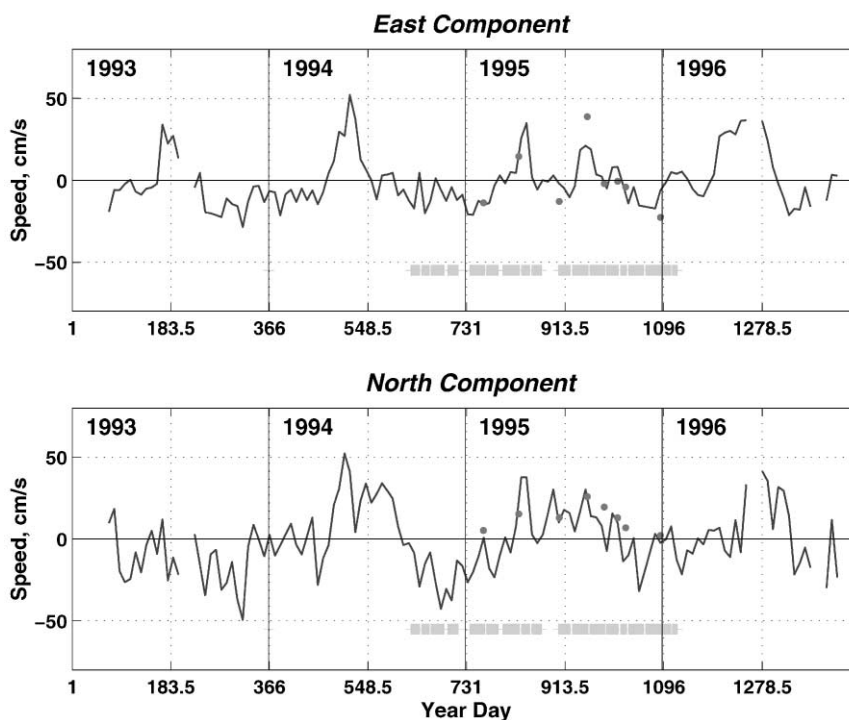
Fig. 7. Comparison of upper-ocean velocities between those derived from the T/P altimeter data (solid line) and the ADCP data at 30 m depth (solid dots). The temporal period of the US JGOFS period is shown in thick lines for each time-series plot. The *x*-axis is year-day with respect to January 1, 1993.

4. Sea-level anomaly derived currents

4.1. Direct comparison with ADCP current measurements

During the Arabian Sea Expedition, the R.V. *Thompson*'s shipboard ADCP measured upper-ocean currents along all the cruise tracks. A number of the cruise tracks traversed the area offshore of the Omani coast approximately under the ascending A1 T/P track (Fig. 1), and near the crossover point with the descending track D2 at 20.6°N, 59.53°E east of Masirah Island (marked as "a"). An evaluation of the SLA-derived velocities is possible by comparing them with ADCP-measured currents from an area within 45 km (the approximate internal Rossby radius) of the crossover point and within ± 5 days of the crossover time. While there were 18 cruises during the Arabian Sea Expedition and more than 20 transits of the area off the Omani coast, there were only eight periods of near-coincident sampling within a Rossby radius of the crossover point. These eight periods were spread fairly evenly throughout 1995 and included times during both the Northeast and Southwest Monsoons (solid circles in Fig. 7). The ADCP measured the upper-ocean currents between the depths of 18 and 426 m, averaging over 5 min intervals while the ship passed through the area. For comparison with the SLA-derived velocities, the ADCP data from the 8 m bin centered at 30 m were used. Tidal currents in the ADCP data could degrade this comparison,

Table 1
A comparison of the T/P-derived near-surface velocities and concurrent ADCP velocities from 30 m (see text) at crossover point "a" located at 20.6°N, 59.53°E. The sample size is eight and the measurements are assumed independent for purposes of calculating the standard errors

Velocity component t	T/P (cm s^{-1})	ADCP (cm s^{-1})	rms differences (cm s^{-1})	r^2
East	1.2 ± 4.4	-0.3 ± 6.8	10.1	0.86
North	6.5 ± 4.5	12.7 ± 2.8	10.6	0.70

although they are not expected to be more than a few cm s^{-1} based upon the moored results from a central Arabian Sea mooring (Weller et al., 1998). At the times of coincident measurements, the east velocity component from the ADCP varied between -22 and 40 cm s^{-1} while the north component varied between 2 and 26 cm s^{-1}. The SLA-derived velocities had a similar range of variability. The two independent observation sets are relatively well correlated with r^2 values of 0.86 and 0.70 for the east and north components, respectively (Table 1). The differences between the east component means are within their standard errors while those for the northern component are not. Nevertheless, the north component means are not statistically significantly different at the 95% confidence level according to a two sample t-test with 13 degrees of freedom. Based upon this comparison, we use the T/P-derived velocities to extend the ADCP observations to other years and locations within the northern Arabian Sea.

4.2. Spatial dependence of SLA-derived current variability

Insight into the temporal variability and velocity response to seasonal wind forcing can be gained by examining four selected SLA-derived velocity time series from crossover points, two along the regional boundaries, one in the central area, and a last one offshore to the south (see labeled crossover points "a" through "d" in Fig. 1). The wind forcing (Fig. 8, top panel) is derived from the pseudo-wind-stress records of FNMOC at the center of area between 10–20°N and 55–65°E (provided by J. Kindle). The velocity series at the crossover points are shown in Fig. 8a–d along with the wind stress, in order to illustrate the relative timing of the current variability and the onset of the monsoon and intermonsoon periods. The wind record clearly indicates the presence of the Northeast and Southwest Monsoons and the short intermonsoon periods in between, with relatively small year-to-year differences over the three years. The SLA-derived velocity near the Omani coast (Fig. 8a) is clearly correlated with the seasonal monsoon signal, particularly in 1994 and 1996 (r^2 greater than 0.5) with little or no lag, suggesting direct forcing by the wind.

It is interesting to note that during 1995, the year of the Arabian Sea Expedition, the monsoonal response at location "a" appears muted relative to the years before and after, but more coherent with the wind than in 1993 during which the current and winds had an $r^2 = 0.4$. Farther to the southwest at location "d", the currents are more vigorous but not as well correlated with the seasonal wind field. In 1994 and 1995, the currents at this location are toward the north/northeast, lagging the Southwest Monsoon by one or two months, occurring at a time when the Northeast
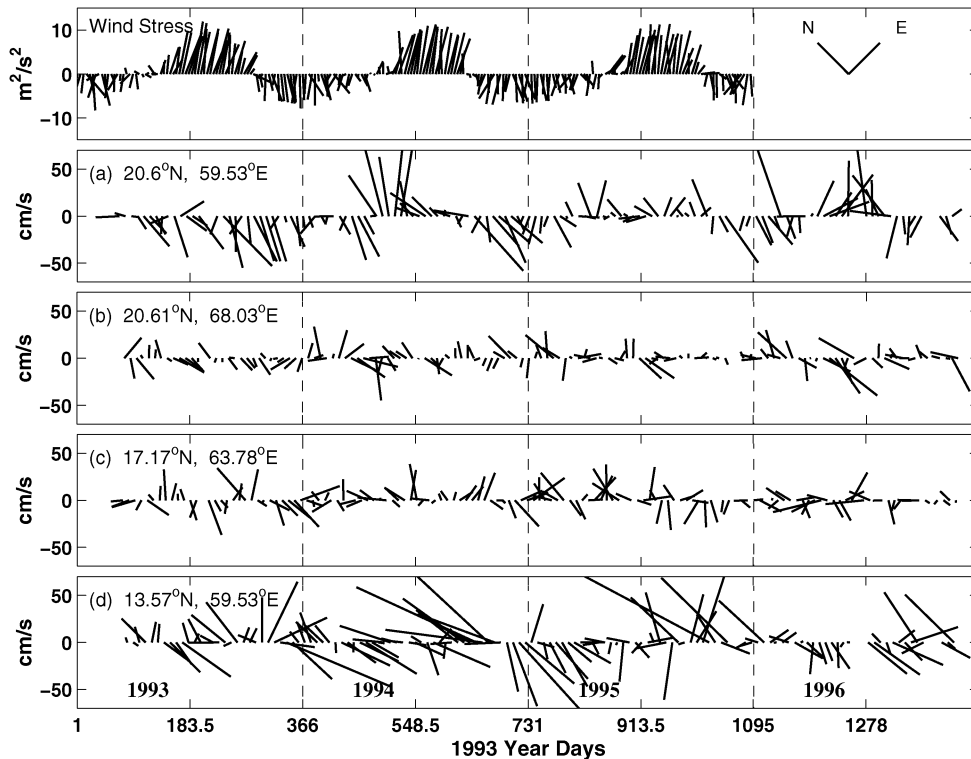
Fig. 8. Time series of winds and SLA-derived velocities. The top panel shows the 5-day interval psuedo-wind stress, and the lower four panels show the SLA-derived currents (9.9156-day interval) at four crossover points shown in Fig. 1: (a) east off Masirah Island, (b) west off Saurashtra, (c) in the central Arabian Sea, and (d) from southwestern portion of the study area.

Monsoon has actually reversed the wind stress toward the southwest. This southwestern crossover point is near the persistent anticyclonic feature identified in FK98 as the Shabatat Anticyclone. Both locations "a" and "d" are northwest of the axis of the atmospheric Findlater Jet (Findlater, 1971), and the kinetic energies there are higher than farther offshore. The other two locations, offshore of the Findlater Jet's axis, are characterized by smaller currents, and they show little coherence with the large-scale wind field. Rather, these records appear to be dominated by small-scale, eddy-like features with time scales on the order of two to three months.

Interannual current fluctuations also appear in the SLA-derived current records, despite the fact that the wind stress follows the same general pattern and variability with much the same magnitude year after year. For example, the currents at locations "a" and "b" north of 20°N appear to be anomalously weak in 1995 compared to 1994 and 1996, and the rms values for the year 1995 are approximately 11–41% smaller than those for the adjacent years (see Table 2). Close to the Omani coast at crossover point "a", the currents during the 1993 Northeast Monsoon are roughly similar to those of the succeeding three years. However, during the 1993 Southwest Monsoon the expected northeastward flow does not materialize and, in fact, the currents appear to have intensified toward the southwest. Similar comments apply to the southwestern crossover point "d", where it appears

Table 2
Annual rms wind stress and current values for the four locations shown in Fig. 8 (units for east and north components are in cm s^{-1}; npts indicates sample size)

	1993	1994	1995	1996
Wind stress				
npts	365	365	365	
East	4.3	5.5	5.0	
North	3.1	4.4	4.0	
Crossover point "a"				
npts	28	36	35	29
East	14.5	17.4	13.0	19.9
North	17.9	25.3	17.1	20.2
Crossover point "b"				
npts	29	36	35	32
East	6.8	8.4	5.9	6.6
North	8.5	13.0	10.5	17.8
Crossover point "c"				
npts	29	36	33	30
East	12.3	11.2	12.9	10.8
North	16.8	12.1	15.8	10.0
Crossover point "d"				
npts	28	36	35	29
East	17.0	16.4	18.5	13.9
North	25.4	39.8	26.2	20.2

that the southwestward flow associated with the onset of the Northeast Monsoon that occurs late in 1994 is completely absent in 1995. In the central part of the basin at "c", the interannual variations seem less marked, although there are year-to-year variations in the strength of the eddies that populate this area. Perhaps, it is because of the slower currents at the area. In terms of rms interannual current variability shown in Table 2, all four sites are roughly equivalent, although not in phase, and their variability is significantly larger than that of the wind field.

The net effect of the seasonal sea-level fluctuations during each of the monsoons is illustrated by the velocities at each of the T/P crossover points in Fig. 9. The upper-ocean velocities for each crossover event within the monsoonal periods show that the inferred currents are highly variable in both speed and direction. The only noticeable difference between the Northeast and Southwest Monsoons is the magnitude of the currents, which are larger during the Southwest Monsoon. Also shown in these figures are the seasonal mean SLA-derived currents and contours of the standard errors of the current amplitudes based upon the root mean squares of the velocity components. Mean currents vary from essentially zero to nearly 20 cm s^{-1} and generally lie along the monsoonal mean SLA isopleths of Fig. 4, as expected. It is immediately obvious that there is little large-scale pattern in the seasonal means except in isolated regions. One such region is along approximately 14°N during the Southwest Monsoon where there is inflow to the region from the southwest, west
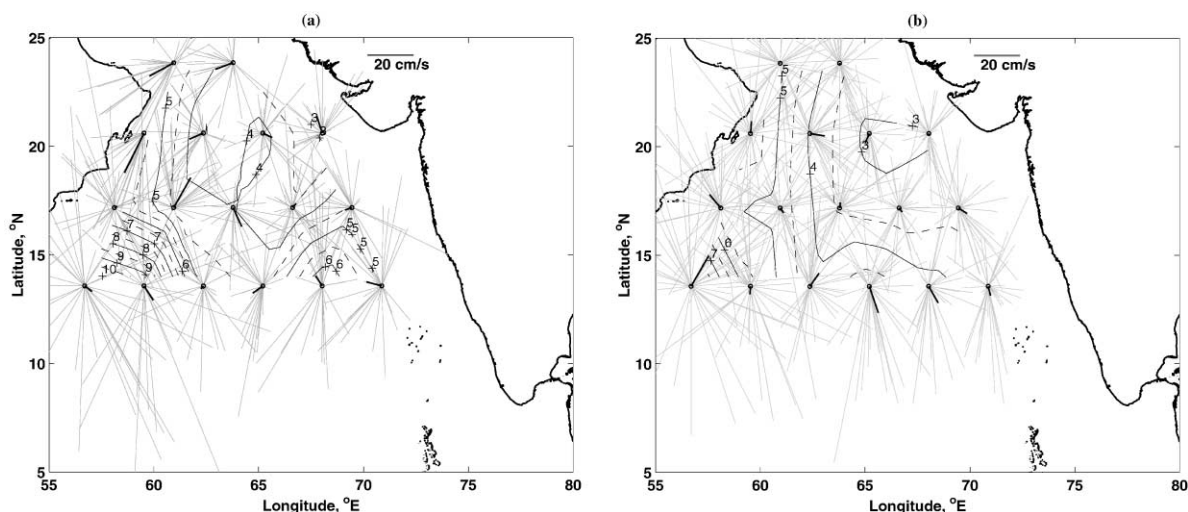
Fig. 9. Upper-ocean seasonal currents for the period of (a) the Northeast Monsoon, and (b) the Southwest Monsoon. The figures show the total velocities at the cross over points for all possible occurrences as light gray vectors and the seasonal averages as bold vectors. The contours show standard error estimates for the seasonal mean velocity magnitudes.

of $\sim 64°$E and a southeastward flow over the eastern portion. However, this pattern does not extend further north into the area.

The overall spatial pattern of current variability is illustrated by a compilation of all the SLA-derived velocities from the 45-month T/P data window at all the crossover points within the northern Arabian Sea. The current roses at each crossover point in the areas are shown in Fig. 10. The highest variability, as marked by the largest current roses, is found to the west and along the Arabian Peninsula, with maximum velocities generally greater than $40\,\text{cm}\,\text{s}^{-1}$ (up to more than $80\,\text{cm}\,\text{s}^{-1}$) at the crossover point about $4°$ south of Ras ash Shabatat. It would appear that the near-coastal variability northeast of Ras al Hadd and east of Masirah Island is anisotropic, with currents oriented more nearly parallel to the shoreline. In contrast, in the southwestern corner and the central area farther offshore, the currents appear moderately isotropic. Even further east, the current ellipses appear to be oriented in a more north–south direction. Toward the east and southeast, variability becomes significantly weaker with the maximum velocities ranging between 30 and $60\,\text{cm}\,\text{s}^{-1}$. Overall, the surface velocity variability is the smallest in the northeastern and central region and increases toward the west and, to a lesser extent, toward the south.

4.3. SLA-derived velocity spectra

Utilizing the functional relationship between the SLA and cross-track velocities V_a and V_d from Eq. (1), the wave number spectra for the cross-track component of the velocities can be estimated by scaling the SLA wave number spectra by a factor of $(g/f)^2\kappa^2$, where κ is the wave number (Stammer, 1997a). This technique reduces spectral noise otherwise accentuated by the finite-difference gradient calculation. The Coriolis parameter used was that from tfhe middle of the area at $17°$N. To further reduce spectral noise, a second-order Butterworth low-pass filter with a 75 km
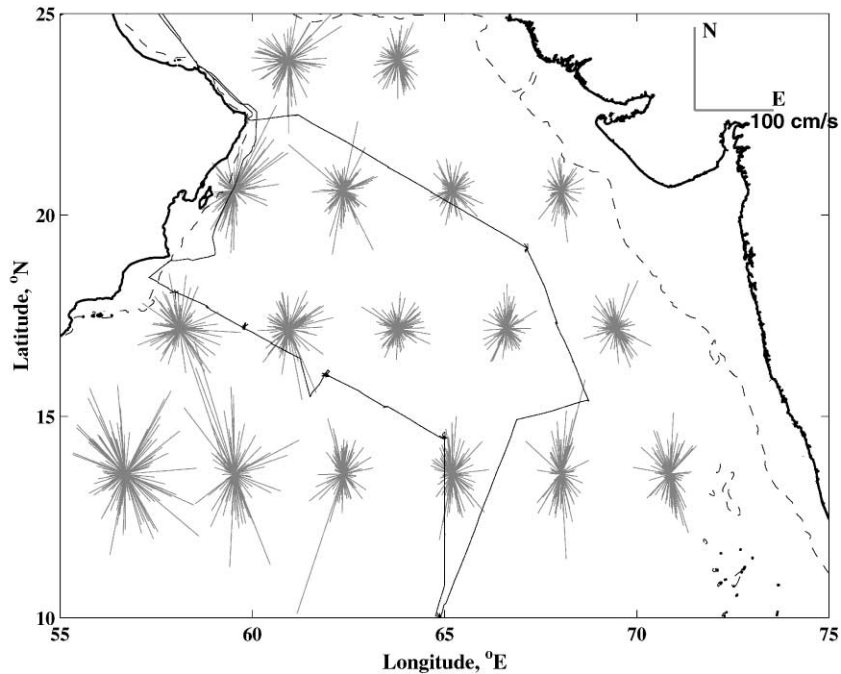
Fig. 10. SLA-derived current roses at 17 crossover points, superimposed on the US JGOFS standard cruise track (solid line) and 200 m isobath (dashed contour). Each current rose covers the period March 1993–November 1996.

cutoff and a 10% cosine taper were applied to the SLA data prior to the Fourier transformations. The low-pass filter strongly attenuates the spectra for wavelengths shorter than ~ 85 km with the result that the spectra shown are limited to wavelengths greater than ~ 100 km. To compensate for the power lost due to the tapering, the resultant spectra were re-scaled by $1/0.875$. The spectra for each T/P track were produced by averaging the spectra for all satellite overflights (~ 133) during the 45-month period.

Fig. 11 shows variance-conserving, cross-track velocity wave number spectra for three ascending and three descending tracks in the region off the Omani coast. The figure indicates that there are significant spectral peaks whose magnitudes and relative importance change both with location and orientation. For the ascending tracks where the cross-track velocities are predominantly offshore, there is a factor of about three decrease in total variance in the offshore direction together with a change from a long-wavelength-dominated system near shore to a much shorter scale eddy field in the central Arabian Sea. Near the coast, the alongshore scale of the offshore flow field is broadly distributed between 200 and 500 km. Some 600 km farther offshore, the variance in this spectral band decreases by a factor of four. Within the wavelength band between 120 and 166 km, there is a barely significant short-wavelength peak near shore, which broadens somewhat offshore while retaining a relatively greater percentage of the variance. Over the same 600 km, the variance within this band decreases by a factor of about two, most of which occurs between tracks A2 and A3, increasing in relative importance from 20 to 35% of the total variance.
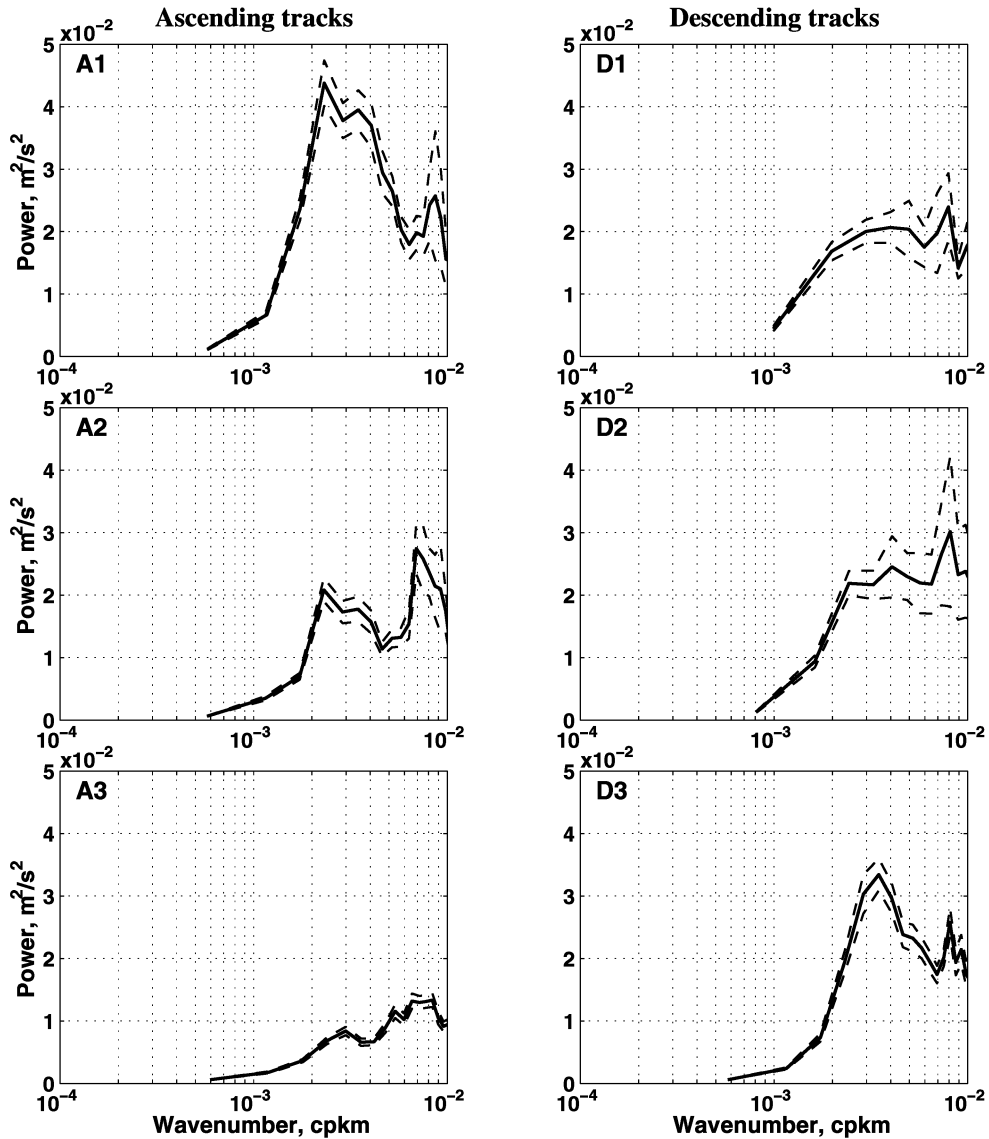
Fig. 11. Average wave number power spectra of cross-track velocities for three ascending tracks A1–A3, and three descending tracks D1–D3. The dashed lines show ± one standard error about the mean spectra.

The wave number spectra for the three descending tracks (D1–D3) represent the scales associated with the structure of the nearly alongshore velocity component. The tracks extend from nearshore to offshore, and each contains elements from all three of the ascending tracks discussed. The variance along all three tracks is about the same with a broad long-wavelength band between 170 and 500 km and a short-wavelength peak at about 125 km that shows up in all three spectra. A reasonable presumption is that the variance in the long-wavelength band originates with the large-scale energetic motions near shore, while the short-wavelength peak is related to the smaller

eddy field that dominates the central Arabian Sea. In addition, track D3, which passes through the Gulf of Oman, shows a strong peak within the long-wavelength band centered at about 280 km. Since this track passes within about 100 km of Ras al Hadd, it is reasonable to assume that this peak is associated with the Ras al Hadd Jet and its strong seasonal fluctuations. Overall, these long-wavelength spectral peaks occur at scales that are very similar to those observed in the near-surface shipboard ADCP data along the US JGOFS transects, typically between 300 and 400 km (FK98).

An examination of the frequency distribution of the cross-track velocities is possible using time series from each of the sub-satellite points. From this data set, cross-track velocity spectra were calculated for the 45-month-long T/P data set at each sub-satellite point. Composite spectra for each track were then obtained by averaging all the spectra along the track. The resulting variance-conserving spectra for the same three ascending (A1–A3) and descending (D1–D3) tracks are presented in Fig. 12. There are minor spectral peaks at a period of approximately 30 days, especially noticeable in the descending tracks, an indication of processing noise in the Poseidon altimeter data (Le Traon et al., 1994). Because of the different orientation of the satellite passes relative to the Arabian coast, the cross-track velocities from the ascending tracks are oriented nearly perpendicular to the coast (onshore/offshore) while those from the descending tracks are oriented largely alongshore.

From the three ascending tracks, the offshore decrease in total variance, shown previously, is again obvious. Although this decrease occurs throughout the frequency range, it is particularly noticeable for periods longer than 50–100 days. In addition, there is a shift in the energy distribution from longer to shorter period fluctuations progressing offshore from tracks A1 to A3. Note that there is only a small spectral peak at near-annual periods for the onshore/offshore velocity from track A1, even though this nearshore area exhibits significant annual variability in the alongshore flow (Fig. 8), captured in the descending track spectra. Farther offshore along track A3, the annual signal is prominent but not as strong as that found in the alongshore flow. There is a strong, nearly semi-annual peak in the A1 ascending track spectrum which does not show up in any of the other spectra except that for D3. The results from the ascending tracks differ markedly from those of the descending tracks, which contain significant energy at annual and semi-annual periods. For periods longer than about 50 days, the spectral amplitudes for the descending tracks are all quite similar, indicating little alongshore dependence. All three of these tracks cross from the most energetic nearshore region to the less energetic interior. The low-frequency energy levels from the descending tracks are somewhat less than those of the inshore A1 line but greater than those from either A2 or A3. The large annual peak is nearly the same for all the descending tracks and clearly represents the response to monsoonal forcing as suggested by the crossover point velocity time series at "a" in Fig. 8. In log–log spectral plots (not shown), the energy density at periods shorter than ~ 100 days appears to follow an f^{-1} dependence, an estimate that is less than that found in highly energetic western boundary current regimes but about the same as found in ocean interiors (Stammer, 1997a). Rotary spectra were also calculated from the velocities at the crossover points "a"–"c", but did not show any significant circular polarization.

4.4. Eddy kinetic energy from the SLA-derived velocities

A comparison of altimeter-derived eddy kinetic energy (EKE) estimates and those derived from the 18-month-long US JGOFS/ONR ADCP data set shows quite reasonable agreement. Because
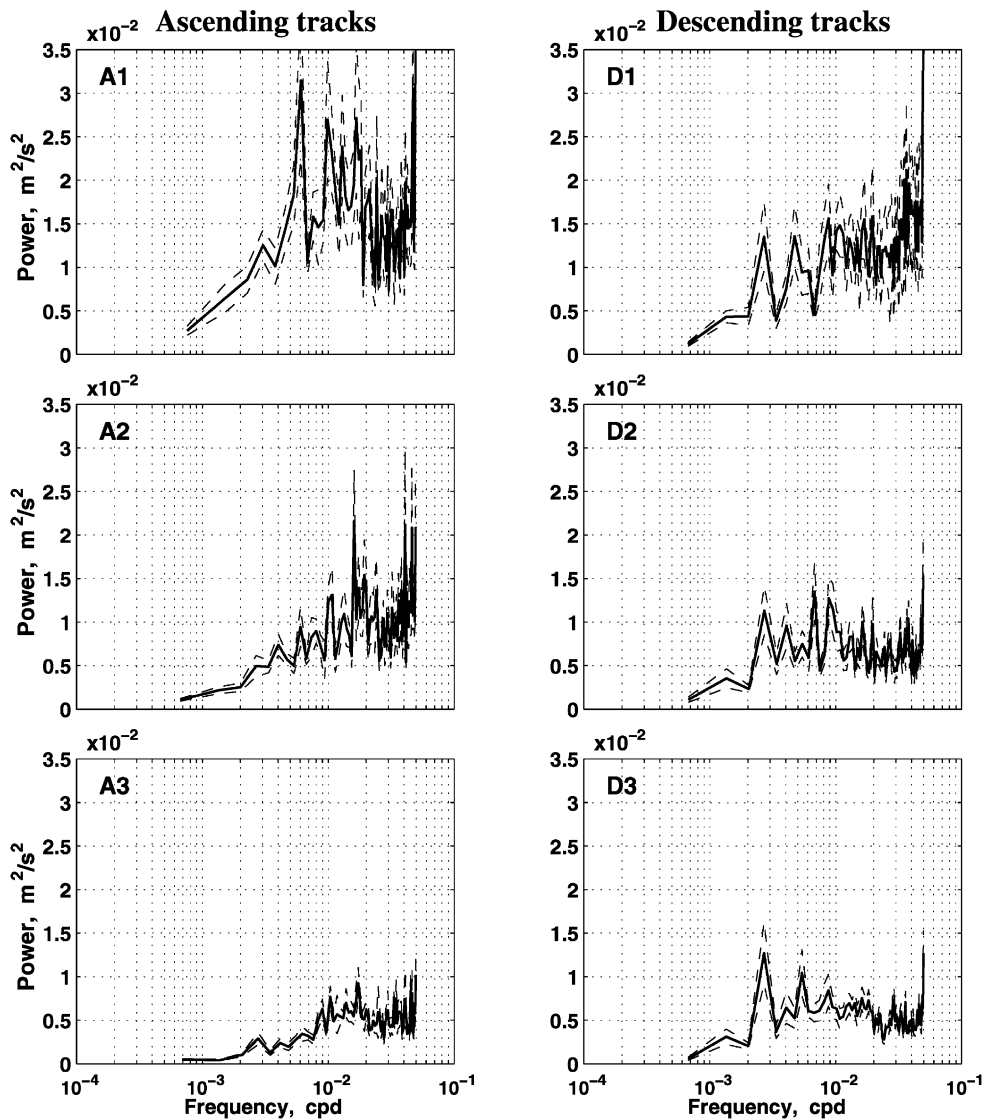
Fig. 12. Energy density frequency spectra of SLA-derived cross-track velocities for ascending tracks (A1–A2) in the left and for descending tracks (D1–D3) in the right. The dashed lines represent ± one standard error.

the mean surface elevation has been removed from the SLA, the SLA-derived total EKE (SLA-EKE) at the crossover points is simply defined as $0.5\langle(u_g^2 + v_g^2)\rangle$. To compare the SLA-EKE with that from the ADCP observations, profiles are obtained along the northern and southern transects by linear interpolation of the gridded SLA-EKE distribution (see Fig. 14). The ADCP-derived EKE profiles come from velocities at 30 m binned into 10 km horizontal intervals. A 200 km boxcar average also was applied to the ADCP-derived EKE profiles for comparison with the less-well resolved SLA-EKE. Fig. 13 shows the offshore EKE profiles from both data sets along the two transects.
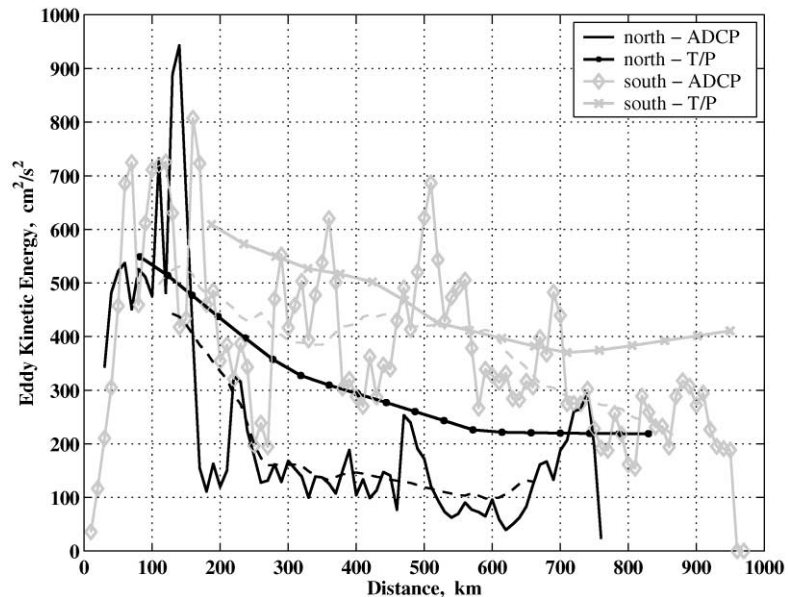
Fig. 13. Profiles of eddy kinetic energy (EKE) along the US JGOFS north and south transects from the ADCP data set (FK98) and the altimeter-derived EKE (solid dark and light curves) subsampled from the EKE contour plot in Fig. 14. Offshore distance is measured from near-coastal points (18.53°N, 57.25°E) for the south and (22.46°N, 59.66°E) for the north. The dashed curves are 21-point running averages of corresponding ADCP-EKE curves.

In FK98, vertical sections showed a surface-intensified kinetic energy distribution in the upper 400 m, acting to concentrate energy in the mixed layer and upper thermocline. Of the total kinetic energy along those sections, more than 90% consisted of eddy kinetic energy. Maximum EKE densities were observed off the edge of the continental shelf in the active nearshore zone of wind-driven currents, coastal squirts, jets and eddies. In the EKE comparison plot, Fig. 13, EKE values range approximately from 200 to 600 cm^2 s^{-2} and from 100 to 500 cm^2 s^{-2} for the SLA-EKE and ADCP-derived estimates (smoothed profiles), respectively. Offshore of the energetic nearshore regime, both sets of EKE profiles show a characteristic offshore EKE decrease. Both data sets also show substantially greater EKE levels along the southern transect as compared to the northern transect. The SLA-EKE values are nearly the same as those derived from the ADCP in the nearshore region but appear to be somewhat larger offshore, overlapping only for some of the peak energy densities observed by the ADCP. It may be that the longer SLA data set, which presumably spans many offshore eddy events, more accurately describes the overall EKE distribution while ADCP-derived results reflect the dominance of a few such events.

Fig. 14 shows the SLA-EKE distribution over the whole northern Arabian Sea for the period March 1993–November 1996. The total SLA-EKE is shown in (a), with the breakdown into its east and north components in (b) and (c), respectively. The resulting SLA-EKE from the four years of data at 20 crossover points have been linearly interpolated to a 1/2° grid. The total EKE ranges from about 150 to 1100 cm^2 s^{-2}. West of 65°E, the EKE isopleths are generally oriented meridionally, while east of that meridian the isopleths become zonal. Thus, the minimum EKEs are found
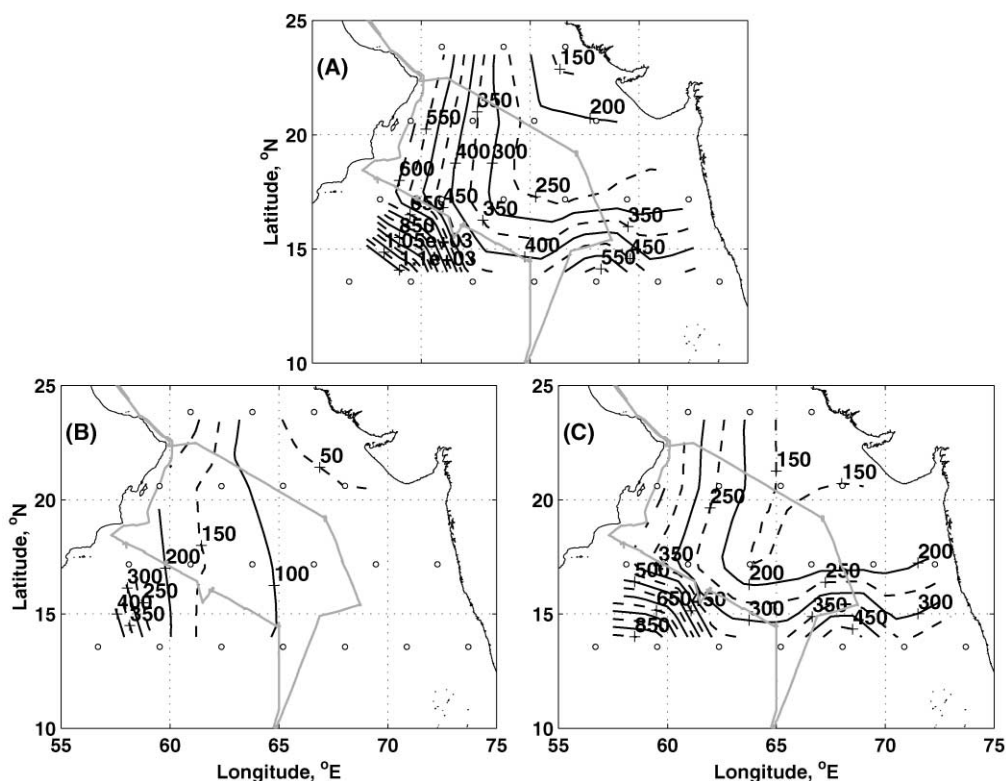
Fig. 14. The spatial distribution of SLA-derived ocean current eddy kinetic energy (EKE) for (a) total EKE, (b) EKE of the east component, and (c) EKE of the north component. The EKE computed at 20 crossover points was interpolated to $1/2°$ grids. The contour intervals for both the dashed and solid lines are $50 \, cm^2 \, s^{-2}$. The open circles represent the T/P altimeter crossover points, and the light line illustrates the nominal US JGOFS cruise track.

along the Indo/Pakistani coast and the greatest energies are found to the west and along the Arabian Peninsula. The largest EKE values, by far, are those found in the southwest. Overall, this pattern looks very much like that of the velocity roses of Fig. 10, as it should. There are interesting differences in the EKEs of the velocity components, Figs. 14b and c. The north component, Fig. 14c, is generally dominant and responsible, in particular, for the zonal character of the isopleths in the southeast portion of the study area.

The large EKE concentration in the southwest portion of the study area occurs in the vicinity of a persistent large anticyclonic eddy feature, referred to as the Shabatat Anticyclone in FK98, that dominated the ADCP records from that region during fall of 1994 and through most of 1995. That this EKE peak shows up so strongly in these diagrams, based upon four years of altimetry data, indicates that while this feature persists from year to year it is also highly variable. Recent numerical model results for the northwestern Indian Ocean circulation (Shankar and Shetye, 1997) reveal that during the Southwest Monsoon the Somali Current and its eddies often extend up to $14°N$ before the majority of the current turns eastward, weakening considerably by the time it

reaches 62°E. The EKE peak ($> 1000 \, \mathrm{cm}^2 \, \mathrm{s}^{-2}$) and the Shabatat Anticyclone, therefore, may reflect the impact of the Somali Current and its extensions, although the connection between these regions is not clear. Eddies shed from the Somali Current do not propagate northward to the coast of the Arabian Peninsula. The secondary region of high EKE values in the southeastern portion of the area off the Indian coast would appear to owe its character to the North Equatorial Current and the Laccadive high formed during the early stages of the Northeast Monsoon and its associated westward planetary wave propagation (Bruce et al., 1994).

5. Discussion and conclusions

We have used the T/P altimetry data to elucidate further the spatial and temporal distribution of current variability in the northern Arabian Sea. The ADCP data set obtained during the US JGOFS/ONR Arabian Sea Expedition indicates that the seasonal currents were dominated by relatively small spatial and short time-scale variability, and that it was difficult to clearly identify seasonal fluctuations, given that overwhelming bias. The impression given was that while some anticipated features of the monsoonal response were visible, such as a downwind current over the shelf and a seasonal Ekman layer response during the Southwest Monsoon, the large-scale downwind currents over most of the Arabian Sea did not manifest themselves. The most important observation, however, was the complete dominance of the currents by the eddy field. The large areal coverage and longer time series available from the T/P overflights permits us to confirm the observation found by the ADCP data and to evaluate the extent to which these concepts apply to the whole of the northern Arabian Sea.

The T/P data confirm both the overall spatial and seasonal current patterns observed by the ADCP. The monsoonally averaged data show the overall, incoherent seasonal mean currents except near the coast, with mean current magnitudes that are an order of magnitude smaller than those predicted from ship-drift observations. The monsoonal mean SLA values show relatively small and seasonally reversing eddy features near the coast between Ras ash Shabatat and east of Masirah Island and off Ras al Hadd, which correspond to the reversing flow field in this area. The lull between these small eddies in the southwestern region and the larger circulation pattern offshore, occurs in an area in which offshore filaments carrying upwelled waters offshore originate. The monsoonally averaged rms SLA values show a great deal of variability within the coastal upwelling region, indicating the high degree of intraseasonal variation due to the generation of squirts, jets and eddies all along the coast. The degree of variability increases in intensity and areal extent during the Southwest Monsoon, the time of greatest winds, and when the coastal, wind-driven flow proceeds with the coast on the left, a situation that favors instabilities and the formation of meanders and eddies similar to those observed off the US west coast. The most energetic eddies lie offshore of the Omani shelf break as the SLA indicates a much reduced level of variability over the shelf itself. The SLA-derived EKE fields are consistent with those derived earlier from the ADCP data in both distribution and magnitude, but provide a better picture of how the offshore EKE gradients along the US JGOFS transects fit into the larger regional energy distribution. There is an increase in EKE to the west and southwest and to a lesser extent to the south, and a large area of relatively reduced eddy activity over much of the eastern and northern Arabian Sea. The spatial scales of the eddies responsible for the EKE distribution range between

200 and 500 km in the nearshore region and decrease to 100–200 km offshore. While there is significant variability on annual and semi-annual time scales, a substantial portion of the energy is found at periods between 50 and 120 days, and the relative importance of this frequency band increases offshore. Lastly, the SLA frequency spectra in the central region indicate a distinct break in the frequency content of the eddy field that occurs at about 15°N with little energy at periods less than annual south of this latitude. This suggests that for some reason the ubiquitous eddies that dominate the current field in the northern Arabian Sea are confined to the area north of 15°N.

One of the more intriguing aspects of the study shows up in the SLA-EKE patterns of Fig. 14 in which there is a large area in the northeastern Arabian Sea of low kinetic energy. The EKE isopleths in this area show a remarkable similarity to the maps of the areal extent of the oxygen minimum zone (OMZ) (Morrison et al., 1998b), or more properly, the extent of the secondary nitrite maximum (Naqvi, 1991) marking the extreme suboxic conditions (see Fig. 1). Not only is the level of kinetic energy lower in this area, but according to the ADCP data (FK98), the area also shows reduced vertical penetration of the eddy field. Together, these suggest that at least part of the reason for the existence of the OMZ in the area, or at least its proximity to the surface, may be the lack of mixing and vertical motion associated with a vigorous eddy field. Clearly, this is not the only factor controlling the OMZ since its vertical extent, ~ 800 m, is much greater than even the ~ 400 m depth of the eddy field off the Arabian Peninsula. But the nitrite plume, where it exists, typically extends from 100 to 400 m and so is definitely within the range of the more energetic coastal eddies. Another issue is how the organic matter that drives the oxidation in the OMZ arrives in this area. It has long been assumed that detrital material generated during the upwelling-driven primary production bloom of the Southwest Monsoon would be swept downwind over a wide area into the OMZ region. Both the ADCP and T/P data indicate that except near the coast, there is no large-scale coherent downwind flow toward the east during the Southwest Monsoon (Fig. 9b). From the ADCP data, the annual average transport in the upper 150 m for all but the coastal region is actually toward the southwest (FK98). Given the evidence to date, the most plausible scenario for transporting biogenic material from the upwelling region into the eastern portion of the OMZ is through a combination of a northeastward coastal flow together with an eastward Ras al Hadd Jet. This appears to be the only way that the material could reach the area other than by horizontal diffusion, which is too slow. The seasonality of the combined northeastward coastal flow and the Ras al Hadd Jet is such that this eastward pathway only exists during the later portion of the Southwest Monsoon (FK98). The distribution of the OMZ seems to match this hypothesis in that it is closest to the surface with the largest vertical extent in the northeast and gets progressively deeper and thinner to the south and to the west. It would seem reasonable, therefore, to suggest that a slow-moving anti-cyclonic circulation exists in the northeastern Arabian Sea between perhaps 800 m and the surface that extends from the Indian shelf to about 62°E and between 12 and 21°N.

Overall, the combination of the altimetry data from the TOPEX/Poseidon project and the ADCP data from the US JGOFS/ONR Arabian Sea project has had a substantial impact on our understanding of the upper-ocean current field of the northern Arabian Sea. This data set forms an important bench mark against which to evaluate the numerical models of the region that will be needed to integrate understanding of all the features of the region.

Appendix. Estimated uncertainty in the altimeter–derived velocities

The estimates of the cross-track velocity V defined in Eq. (1) were made using a centered-difference approximation (Ames, 1977):

$$V(i) = \frac{g}{f}\left(\frac{\eta(i+1) - \eta(i-1)}{2\Delta}\right), \tag{A.1}$$

where $V(i)$ is the estimate at grid point i, Δ is the along-track spacing between the adjacent points $(i+1)$ and $(i-1)$, and η is the SLA along the ascending or descending track. The approximation Eq. (A.1) is subject to two types of errors; a truncation error, σ_N, and a measurement error, σ_M. The σ_N is the largest remainder term from the Taylor expansion, given by

$$\sigma_N \approx \frac{g}{f}\frac{\Delta^2}{6}\eta''',$$

where η''' is the third-order derivative of η, and σ_M is related to the T/P altimeter error $\delta\eta$ which propagates through the differential operator as follows:

$$\sigma_M \approx \frac{g}{f}\frac{\delta\eta}{\sqrt{2}\Delta}.$$

Assuming that σ_N and σ_M are independent, the total uncertainty in the cross-track velocity estimate of Eq. (A.1) is

$$\delta V_\eta \approx (\sigma_N^2 + \sigma_M^2)^{1/2}.$$

The two constituent error estimates have an opposing dependency on Δ, indicating that the total error will have a minimum at some intermediate value of Δ. Observations suggest that a typical value for $|\eta'''|$, based upon the unfiltered SLA, would be $\sim 0.5 \times 10^{-19}\,\text{cm}^{-2}$ using a distance of $O(10\,\text{km})$ for Δ, while $\delta\eta \sim 3\,\text{cm}$. Since σ_N increases quadratically and σ_M decreases inversely with Δ, the minimum total error occurs at a spacing of $\Delta \approx 60\,\text{km}$. At this separation the total estimated cross-track velocity error δV is $\sim 9\,\text{cm s}^{-1}$. The 75 km smoothing of the SLA prior to the velocity computation reduces the rms velocity error approximately by $\sim 22\%$. Hence, the magnitude of uncertainty δV is finally on the order of $7\,\text{cm s}^{-1}$. This estimate for δV is very similar to the square root value of the error variance found from the T/P cross-track velocities and current meter mooring data set by Strub et al. (1997).

The uncertainty for the total SLA-derived velocity $\vec{V}_g$ can be determined from estimates of east and north component errors, δu_g and δv_g, from the relation $\vec{V}_g = u_g\hat{i} + v_g\hat{j}$. Because each

orthogonal component is related to V from either Eq. (2) or Eq. (3), the error in the east component, δu_g, for example, is given by:

$$\delta u_g = \left[\left(\frac{du_g}{dV_a}\delta V_a\right)^2 + \left(\frac{du_g}{dV_d}\delta V_d\right)^2 + \left(\frac{du_g}{d\cos\theta}\delta(\cos\theta)\right)^2\right]^{1/2},$$

$$= \frac{1}{2}\left[\left(\frac{\delta V_a}{\cos\theta}\right)^2 + \left(\frac{\delta V_d}{\cos\theta}\right)^2 + \left((V_a - V_d)\frac{\sin\theta\,\delta\theta}{\cos\theta}\right)^2\right]^{1/2}.$$

An error source not shown in the equation above is that due to the crossover time difference between ascending and descending tracks and lack of synopticity. In the Arabian Sea the crossover time difference is about 4.5 days. Because this difference is substantially shorter than the first zero-crossing time (~ 40 days), the error variation due to the sampling time difference should be minor. Using $\theta = 21.5°$ and $\delta\theta = 1°$, the magnitude of the third term on the right-hand side is estimated to be of the order $0.5\,\mathrm{cm\,s^{-1}}$ for typical values of 10 and $50\,\mathrm{cm\,s^{-1}}$ for $V_a - V_d$ and $V_a + V_d$, respectively. This is significantly smaller than the other two terms. Therefore, the equation above can be approximated as

$$\delta u_g \approx \frac{\delta V}{\sqrt{2}\cos\theta}.$$

Similarly, the north component error δv_g is

$$\delta v_g \approx \frac{\delta V}{\sqrt{2}\sin\theta}.$$

Using $\delta V = 7\,\mathrm{cm\,s^{-1}}$ and $\theta = 21.5°$, δu_g and δv_g are 5.4 and $13.3\,\mathrm{cm\,s^{-1}}$, respectively. Assuming δu_g and δv_g are independent, the total uncertainty δV_g, expressed as $(\delta u_g^2 + \delta v_g^2)^{1/2}$, is $\sim 14\,\mathrm{cm\,s^{-1}}$.

References

Ames, W., 1977. Numerical Methods for Partial Differential Equations. Academic Press, New York, 365pp.

Blayo, E., Verron, J., Molines, J.M., 1994. Assimilation of TOPEX/Poseidon altimeter data into a circulation model of the North Atlantic. Journal of Geophysical Research 99 (24), 24691–24705.

Böhm, E., Morrison, M., Manghnani, V.J.A., Kim, H.-S., Flagg, C.N., 1999. Remotely sensed and acoustic Doppler observations of the Ras al Hadd jet in 1994–1995. Deep-Sea Research II 46, 1531–1549.

Bruce, J.G., Johnson, D.R., Kindle, J.C., 1994. Evidence for eddy formation in the eastern Arabian Sea during the Northeast Monsoon. Journal of Geophysical Research 99, 7651–7664.

Brink, K., Arnone, R., Coble, P., Flagg, C.N., Jones, B., Kindle, J., Lee, C., Phinney, D., Wood, M., Yentsch, C., Young, D., 1998. Monsoons boost biological productivity in the Arabian Sea. Eos, Transactions of the American Geophysical Union 79, 168–169.

Bruce, J.G., 1983. The wind field in the western Indian Ocean and the related ocean circulation. Monthly Weather Review 111, 1442–1452.

Bruce, J.G., Kindle, J.C., Kantha, L.H., Kerling, J.L., Bailey, J.F., 1998. Recent observations and modeling in the Arabian Sea Laccadive High region. Journal of Geophysical Research 103 (4), 7593–7600.

Cutler, A.N., Swallow, J.C., 1984. Surface currents of the Indian Ocean (to 25°S, 100°E). Technical Report, Institute of Ocean Sciences, Wormley, England, 187pp.

Findlater, J., 1971. Mean monthly airflow at low levels over the western Indian Ocean. Geophysical Memoirs London 16, 1–53.

Flagg, C.N., Kim, H.-S., 1998. Upper ocean currents in the northern Arabian Sea from shipboard ADCP measurements collected during the 1994–1996 JGOFS and ONR programs. Deep-Sea Research II 45, 1917–1959.

Gundersen, J.S., Gardner, W.D., Richardson, M.J.M., Walsh, I.D., 1998. Effects of monsoons on the seasonal and spatial distributions of POC and chlorophyll in the Arabian Sea. Deep-Sea Research II 45, 2103–2132.

Hastenrath, S., Greischar, L., 1991. The monsoonal current regimes of the tropical Indian Ocean: observed surface flow fields and geostrophic and wind-driven components. Journal of Geophysical Research 96, 12619–12633.

Koblinsky, C.J., Beckley, B.D., Ray, R.D., Wang, Y.-M., Tsaoussi, L., Brenner, A., Williamson, R., Raytheon STX Corporation, 1998. NASA Ocean Altimeter Pathfinder Project. Report 1: Data Processing Handbook. NASA Memorandum TM-1998-208605, Goddard Space Flight Center, Greenbelt, MD 20771, 54pp.

Krishnamurti, T.N., 1981. Cooling of the Arabian Sea and the onset-vortex during 1979. Recent Progress in Equatorial Oceanography: A Report of the Final Meeting of SCOR Working Group 47. Nova University/N.Y.I.T. Press, Dania, FL, pp. 1–12.

Lee, C.M., Jones, B.H., Brink, K.H., Fisher, A., 1999. The upper ocean response to monsoonal forcing in the Arabian Sea: seasonal and spatial variability. Deep-Sea Research II 47, 1177–1226.

Le Traon, P.Y., Stum, J., Dorandeu, J., Gaspar, P., Vincent, P., 1994. Global statistical analysis of TOPEX and POSEIDON data. Journal of Geophysical Research 99, 24619–24631.

Manghnani, V., Morrison, J.M., Hopkins, T.S., Bohm, E., 1998. Advection of upwelled waters in the form of plumes off Oman during the Southwest Monsoon. Deep-Sea Research II 45, 2027–2052.

Morrison, J.M., Codispoti, L.A., Gaurin, S., Jones, B., Manghnani, V., Zheng, Z., 1998a. Seasonal variation of hydrographic and nutrient fields during the US JGOFS Arabian Sea Process Study. Deep-Sea Research II 45, 2053–2102.

Morrison, J.M., Codispoti, L.A., Smith, S.L., Wishner, K., Flagg, C.N., Gardner, W.D., Gaurin, S., Naqvi, S.W.A., Manghnani, V., Prosperie, L., Gundersen, J.S., 1998b. The oxygen minimum zone in the Arabian Sea during 1995. Deep-Sea Research II 46, 1903–1932.

Naqvi, S.W.A., 1991. Geographical extent of denitrification in the Arabian Sea in relation to some physical processes. Oceanologica Acta 14, 281–290.

Nerem, R.S., Schrama, E.J., Koblinsky, C.J., Beckley, B.D., 1994. A preliminary evaluation of ocean topography from TOPEX/POSEIDON mission. Journal of Geophysical Research 99 (12), 24565–24583.

Pickard, G.L., Emery, W.J., 1990. Descriptive Physical Oceanography: An Introduction. Pergamon Press, New York, 320pp.

Rudnick, D.L., Weller, R.A., Eriksen, C.C., Dickey, T.D., Marra, J., Langdon, C., 1997. Moored instruments weather Arabian Sea Monsoons, yield data. Eos, Transactions of the American Geophysical Union 78, 117–121.

Schott, F., 1983. Monsoon response of the Somali Current and associated upwelling. Progress in Oceanography 2, 357–381.

Shankar, D., Shetye, S.R., 1997. On the dyanmics of the Lakshadweep high and low in the southeastern Arabian Sea. Journal of Geophysical Research 102 (6), 12551–12562.

Shetye, S.R., Gouveia, A.D., Shenoi, S.S.C., Michael, G.S., Sundarm, D., Almerida, A.M., Santanam, K., 1991. The coastal current of western India during the northeast monsoon. Deep-Sea Research 38, 1517–1529.

Smedstad, O.M., Fox, D.N., 1994. Assimilation of altimeter data in a twolayer primitive equation model of the Gulf Stream. Journal of Physical Oceanography 24, 305–325.

Stammer, D., 1997a. Global characteristics of ocean variability estimated from regional TOPEX/POSEIDON altimeter measurements. Journal of Physical Oceanography 27, 1743–1769.

Stammer, D., 1997b. Steric and wind-induced changes in TOPEX/POSEIDON large-scale sea surface topography observations. Journal of Geophysical Research 102 (9), 20987–21009.

Strub, P.T., Chereskin, T.K., Niiler, P.P., James, C., Levine, M.D., 1997,. Altimeter-derived variability of surface velocities in the California Current System: 1. Evaluation of TOPEX altimeter velocity resolution. Journal of Geophysical Research 102 (6), 12727–12748.

Weller, R.A., Baumgartner, M.F., Josey, S.A., Fischer, A.S., Kindle, J.C., 1998. Atmospheric forcing in the Arabian Sea during 1994–1995: obervations and comparisons with climatology and models. Deep-Sea Research II 45, 1961–2000.